ROYAL SOCIETY
OF CHEMISTRY

PAPER

Unraveling multi-level porous carbon negative electrode materials based on *Rosa roxburghii* pomace for high-performance sodium-ion batteries

Fangli Lou,[a] Jinju Wang,[a] Xiang Wang,[a] Mingxian Zhang[b] and Jie Yuan ⓘ *[b]

A key hurdle in optimizing sodium-ion battery (SIB) performance is developing cost-effective, highly stable anode materials. Biomass-derived carbon has emerged as a leading candidate due to its recyclability and structural benefits. As a cellulose-rich biomass waste, *Rosa roxburghii* pomace (RRP) can be transformed into hard carbon materials with porous structures and suitable interlayer spacing through carbonization and structural regulation, exhibiting excellent sodium storage performance. In this study, we developed high-performance hard carbon materials through a straightforward thermal decomposition method, starting with RRP as the primary feedstock. To fine-tune the structure, melamine served as a nitrogen source, effectively weaving nitrogen heteroatoms into the carbon framework. Boasting a sizable interlayer carbon distance (0.69 nm), RRP-800-N exhibits a remarkable reversible capacity (223.7 mAh g^{-1} at 31 mA g^{-1}). It also showcases a high initial coulombic efficiency, clocking in at 99.11% at 31 mA g^{-1}, and demonstrates a stable cycling life, retaining 237.1 mAh g^{-1} after 100 cycles at 31 mA g^{-1}. The experimental results indicate that the high-activity N groups and disordered amorphous structure of RRP-800-N offer sufficient active sites and enhance conductivity. In addition, the abundant mesopores provide continuous ion transport pathways, shortening the diffusion distance of Na$^+$ from the electrolyte to the bulk material. This research shows how RRP biomass waste can be transformed into affordable, sustainable hard carbon, proving its potential as a durable sodium-ion battery anode.

1 Introduction

As the global economy expands rapidly, the swift advancement of solar, wind, and other renewable energy sources has increased the need for efficient energy storage solutions.[1,2] Lithium-ion batteries (LIBs) exhibit high cycling endurance excellent rate performance and high energy density. Therefore, these batteries are deemed highly fitting for energy storage applications, extensively employed in substantial systems such as smart grids and e-vehicles.[3–6] However, the limited reserves and uneven distribution of lithium resources pose a challenge to the ever-increasing demand for LIBs. Given the abundance, low cost, and high availability of sodium (Na) resources compared to lithium, there is a pressing need to investigate promising renewable energy storage devices. Since the electro-chemical behavior of the two is similar, SIBs are regarded as the most suitable candidate.[7] Sodium ions (Na$^+$), which have an ionic radius of 1.02 Å, are significantly larger than lithium ions

(0.76 Å). This size difference creates substantial challenges for sodium-ion batteries (SIBs), negatively impacting their cycling stability, electrochemical kinetics, and rate capability.[8,9] Hence, investigating optimal electrode materials and advancing high-performance SIBs with superior rate capability, durability and energy density is crucial.

Hard carbon materials have an interlayer spacing of 0.38 nm. The interlayer spacing of hard carbon is typically larger, significantly exceeding that of graphite, due to the highly disordered arrangement of its microcrystallites and the presence of numerous defects and curved structures between the layers. *Rosa roxburghii* pomace is a biomass source, and biochar typically has an even larger interlayer spacing than hard carbon, potentially much greater. This is due to the natural complexity of its precursor (biomass) and a lower degree of graphitization.[6,10,11] Biomass-based carbon materials, a type of hard carbon, have even larger interlayer spacing and more active sites, which are conducive to the passage of Na ions and the penetration of electrolytes.[12] A diverse range of biomass sources, including coconut shells,[13] lotus roots,[14] orange peel,[15] and rapeseed[16] consistent quality, these substances may substantially lower sodium-ion battery expenses, facilitating mass production.[17] Biomass-derived carbon materials, a robust form

[a]College of Environmental and Chemical Engineering, Dalian University, Dalian, Liaoning, 116622, China

[b]School of Chemistry and Materials Engineering, Liupanshui Normal University, Liupanshui, Guizhou, 553004, China. E-mail: yuanjieedu@163.com

of hard carbon, boast wider interlayer spacing and a greater number of active sites. This facilitates the movement of sodium ions and the permeation of electrolytes, paving the way for improved performance. A diverse range of biomass sources, including coconut shells, lotus roots, orange peels, and rapeseed, are showing promise as anode materials. Due to their abundance, low cost, consistent quality, and ease of preparation, these materials could significantly reduce the cost of sodium-ion batteries and really get them ready for large-scale production. The cost can be further reduced and the performance can be improved by optimizing the precursor and preparation process.[18] Nonetheless, biocarbon anodes currently suffer from limited capacity, diminished rate capability, and reduced first-cycle efficiency. To address these issues, Pei et al.[19] prepared hard carbon materials from discarded tea leaves using a simple carbonization method. When tea leaves were pyrolyzed at 1400 °C, the processed substance exhibited a recoverable charge capacity of 282.4 mAh g^{-1} at 0.1C. Despite this promising performance, its initial coulombic efficiency (ICE) of just 69% falls short of the standards needed for commercial anode applications. In contrast. Xie et al.[20] produced carbon dots from hydrothermal carbonization byproducts, achieving an impressive 300 mAh g^{-1} capacity in sodium-ion batteries. Their material also boasted a dramatically improved ICE of 91% at 30 mA g^{-1}. While these results are noteworthy, the synthesis process for this high-efficiency hard carbon remains prohibitively complex and expensive for large-scale production. Thus, its commercial application will be more difficult. Jeon et al.[21] developing carbon-based materials from onions, achieving a high specific surface area in both the dried onion (DO) and freeze-dried onion (FDO) forms. This was accomplished by starting with onions as the primary source and integrating freeze-drying techniques with potassium hydroxide (KOH) processing. At the 30th cycle, discharge efficiencies reached 140.5 mAh g^{-1} for DO and 151.4 mAh g^{-1} for FDO respectively. At 30 A g^{-1}, battery charge/discharge capacities are limited to 45 (DO) and 66 (FDO) mAh g^{-1}, respectively. Through a complex process, the resulting specific capacity is low, which makes it difficult to meet the demand of the market for anode materials with high specific capacity.

Addressing these challenges an N-doped *Rosa roxburghii* pomace (RRP)-based hard carbon (RRP-800-N) was proposed in this study. *Rosa roxburghii* pomace was carbonized in a tube furnace at a carbonization temperature of 800 °C, resulting in the sample RRP-800, and then nitrogen atoms were introduced into RRP-800, followed by secondary carbonization to obtain RRP-800-N. The sodium storage performance was optimized by expanding interlayer spacing and introducing active sites through heteroatom doping combined with a closed-pore structure. This material tackles the problems of low capacity and insufficient ICE of traditional biomass hard carbon *via* the synergistic effect of pore structure regulation and heteroatoms while having the advantages of low cost (biomass waste feedstocks) and scalability potential. Future research should investigate how closed pores form and determine the ideal doping ratios to advance sodium-ion battery (SIB) node materials for market use.

2 Experiment

2.1 Materials and reagents

RRP-based samples were collected in Guizhou Province. After the *Rosa roxburghii* pomace was rinsed with water, the samples were dried in a 110 °C oven for 12 hours. The dried *Rosa roxburghii* pomace was crushed using a grinder. The RRP that passed through a 20-mesh sieve was selected and then ball-milled into a fine powder using a YXQM-0.4L planetary ball mill at 800 rpm. The RRP that passed through a 100-mesh sieve was chosen for use. Melamine was provided by Aladdin Chemical Co, Ltd (Shanghai, China).

2.2 Material synthesis

2.2.1 Preparation of PPR-800. The RRP was washed with deionized water several times and then placed in a 110 °C vacuum oven for overnight drying. Subsequently, the dried RRP was crushed using a grinder and then ball-milled into a fine powder using a YXQM-0.4L planetary ball mill at 800 rpm. The RRP passing through a 100-mesh sieve was selected for use. Finally, the RRP underwent pyrolysis at 800 °C for 2 h in Ar, ramped at 10 °C min^{-1}, yielding RRP-800.

2.2.2 Preparation of RRP-800-N. In a controlled experiment, RRP-800 was blended with melamine, a nitrogen source, at a precise 1 : 0.5 ratio. This mix was then carbonized at a sizzling 800 °C for a solid two hours in an argon-rich environment, with the temperature rising at a leisurely pace of 10 °C min^{-1}. The new compound, dubbed RRP-800-N, emerged from the process. You can find a snapshot of the procedure in Fig. 1.

2.3 Material characterization

Thermal decomposition was assessed *via* Netzsch STA 449 under argon, with a heating pace of 10 °C min^{-1}. The crystallographic structure of the produced materials was examined *via* X-ray diffraction on a Rigaku MiniFlex 600, with a scanning rate of 10 °C min^{-1}, covering the range of 10 to 80°. Raman spectroscopy is a technique used to study the chemical composition, crystal structure, and defect states of materials by analyzing

Fig. 1 Experimental flow chart for the preparation of RRP-800 and RRP-800-N.

their molecular vibrations and crystal structure, with the Thermo Scientific DXR2xi instrument in the United States (USA) emitting a laser beam at 455 nanometers. The valence states and chemical bond arrangements in the samples were probed with X-ray photoelectron spectroscopy, using a Thermo Fisher Nexsa system. The samples' morphology was meticulously observed and characterized with both scanning electron microscopy (SEM) on a Hitachi cold field Regulus8230 and transmission electron microscopy (TEM) on a FEI Tecnai F20. Fourier transform infrared spectra were acquired with an FTIR from Thermo Nicolet iS5. The specific surface area was determined using the Brunauer–Emmett–Teller (BET) method, based on nitrogen adsorption isotherms obtained at 87 kelvin within an Ar adsorption setup from TriStar II 3020 2.00.

2.4 Electrochemical testing

A finely blended slurry was concocted by combining the active ingredient, acetylene black, and polyvinylidene fluoride (PVDF) in a $8:1:1$ weight proportion within 1-methyl-2-pyrrolidone (NMP). This mixture was then applied to aluminum foil to create the electrodes. The electrodes had an active material loading of roughly 1.5 to 2 mg cm^{-2}. For the counter electrode in the electrochemical tests, sodium metal was employed. The coin cells, CR2032, were put together in an argon-filled glove box where the oxygen and water levels were less than 0.1 parts per million. Glass fiber (Whatman GF/D) served as the separator, while the electrolyte was a 1 M solution of sodium perchlorate (NaClO$_4$) dissolved in a $1:1$ mix of ethyl cellulose (EC) and diethyl carbonate (DEC). The cells' specific capacity, cycling efficiency, and charge–discharge capabilities were assessed with a Land 3002A device within a voltage spectrum from 0 to 2.5 volts. The GCD process involved discharging the battery down to 0 volts followed by charging it back up to 2.5 volts, and this sequence was cycled. Cyclic voltammetry was used to evaluate the sodium-ion half-cells, with data gathered using a VersaSTAT3 electrochemical workstation. The scan rate was set at 0.1 mV s^{-1}, and the voltage window ran from 0.4 to 2.5 V (vs. Na/Na$^+$). On top of that, we performed electrochemical impedance spectroscopy (EIS), sweeping frequencies from 0.01 Hz all the way up to 100 kHz, using a 5 mV amplitude.

3 Results and discussion

The microscopic morphology of the Rosa roxburghii pomace and nitrogen-doped biochar was observed, as shown in Fig. 2a and b. Both samples display a blocky morphology, and an irregular blocky appearance could be observed, this material offers ample room for the electrolyte solution to spread and seep in. It turns out that the surface conditions of both RRP-800 and RRP-800-N are quite alike, suggesting that there's no major alterations in the shapes and internal structure of these carbon substances, nor in the robustness of the Rosa roxburghii pomace framework. RRP-800-N boasts a surface that is riddled with more holes, which suggests that N doping has a certain impact on the surface structure of the Rosa roxburghii pomace and more pores also provide more space for the diffusion and penetration of the
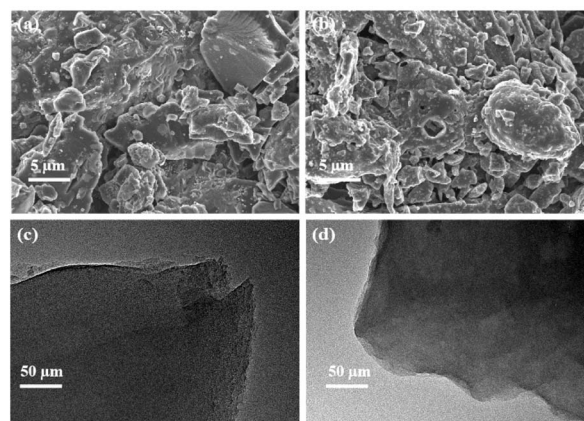

Fig. 2 Scanning electron microscopy (SEM) images: (a) RRP-800; (b) RRP-800-N; transmission electron microscopy (TEM) images; (c) RRP-800; (d) RRP-800-N.

electrolyte. To further confirm the morphology, TEM images were provided. As illustrated in the TEM images of RRP-800 and RRP-800-N (Fig. 2c and d), this carbon sheet with irregular density features particles of varying density. This loose blocky structure greatly contributes to the electrochemical Na$^+$ adsorption/desorption process.[22]

The XRD patterns of the Rosa roxburghii pomace hard carbon (RRP-800) and N-doped hard carbon material (RRP-800-N) are presented in Fig. 3a. XRD scans reveal two wide maxima centered around 24° (002) and 44° (100), which reveals that both samples have a disordered amorphous structure,[23] with a small amount of crystalline carbon produced during carbonization. RRP-800-N exhibits a weaker diffraction peak on the (100)
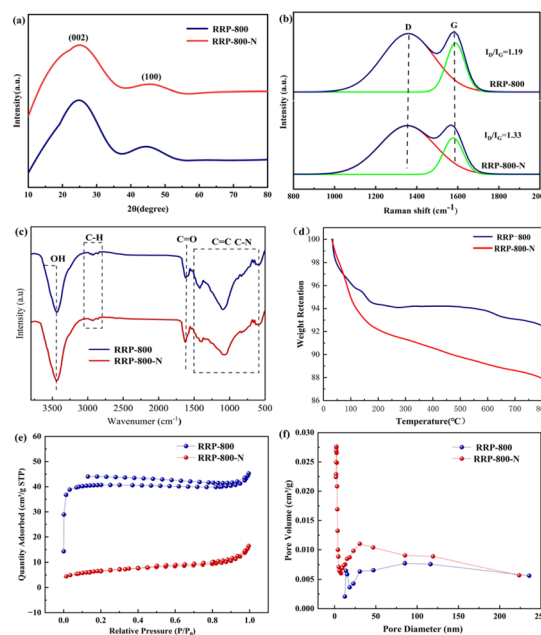

Fig. 3 (a) XRD patterns; (b) Raman spectrum; (c) Fourier transform infrared (FTIR) spectrum; (d) thermogravimetric analysis (TGA) curve; (e) N$_2$ adsorption–desorption isotherm; (f) pore size distribution plot.

crystal plane in comparison with RRP-800, which suggests a decrease in its crystallinity. Melamine addition caused a redshift in the (002) crystal plane's diffraction peak, which indicates a marked increase in interlayer spacing. Through XRD calculations, the PPR-800-N material boasts a notably wider interlayer spacing of 0.69 nm, as opposed to the 0.66 nm found in RRP-800, a difference that can be credited to the incorporation of heteroatoms. The larger interlayer spacing of RRP-800-N can reduce the resistance to intercalation and decrease volume changes, thereby improving cycle stability.[24] This expanded gap between carbon layers enhances the sodium ion's mobility. Additionally, the peak's widening is a direct result of the material's porous nature, which limits the crystallization of the graphite walls.[6,25] In RRP-800-N, melamine-derived nitrogen doping decomposes during high-temperature pyrolysis, generating nitrogen-containing free radicals (such as NH_3 and HCN). The nitrogen atoms are incorporated into the carbon layers through the following mechanism, nitrogen atoms insert between the carbon layers, and the lone pair electrons of pyridinic nitrogen (N-6) and pyrrolic nitrogen (N-5) repel the π electron cloud of the carbon layers, weakening the van der Waals forces between the layers and leading to an expansion of the interlayer spacing.[26]

To better observe the introduction of N atoms, Raman spectroscopy characterization was performed on the *Rosa roxburghii* pomace hard carbon material. Raman spectra typically assess graphitic order and defects in hard carbon anode materials. Distinct peaks for the D and G bands emerge around 1355 and 1591 cm^{-1} (Fig. 3b), respectively. The full width at half maximum (FWHM) of the D peak in RRP-800-N expands and its position migrates to a lower wavenumber, indicating the introduction of N atoms. Typically, the D band signifies the carbon lattice's defect density, the G band indicates hard carbon's graphitization. The intensity ratio between the D and G bands provides insight into the carbon's amorphousness level. RRP-800 and RRP-800-N exhibited I_D/I_G ratios of 1.19 and 1.33, both exceeding unity, which signifies that the graphene flakes in these two materials have large defects.[27] The I_D/I_G ratio of RRP-800-N is higher than that of RRP-800. This indicates that the RRP-800-N material has more defects, which can provide more active sites. Compared to the undoped RRP-800, the nitrogen atoms in RRP-800-N are embedded into the carbon network in the form of pyridinic nitrogen (N-6) and pyrrolic nitrogen (N-5), disrupting the continuity of sp^2 carbon and forming topological defects (such as five-membered rings and seven-membered rings). This increases the defect density of RRP-800-N.[28] The disrupted arrangement aligns with the XRD findings. The FTIR curves of RRP-800 and RRP-800-N are demonstrated in Fig. 3c. It can be seen that the *Rosa roxburghii* pomace has completed the doping of N atoms and its transformation into carbon. Several typical characteristic peaks can be detected, with carbonyl (C=O) and hydroxyl (O–H) groups corresponding to characteristic absorption peaks at 1630 and 3430 cm^{-1}, respectively. RRP-800-N exhibits elevated carbonyl levels relative to RRP-800.[29]

Thermogravimetric (TGA) profiles of RRP-800 and RRP-800-N under N_2 atmosphere (30–800 °C, Fig. 3d) reveal their thermal degradation behaviors. PPR-800-N showed a 5.92% mass loss between ambient temperature and 120 °C, resulting from the desorption of physisorbed/chemisorbed water and evaporation of low-molecular-weight organic species. Thermal treatment between 120–290 °C induced a 4.74% mass loss, attributed to the decomposition of labile organic components and nascent carbon framework formation. Between 290 and 580 °C, a final mass loss of 2.01% was observed, likely due to the combustion and decomposition of the carbonaceous material. The residues after the combustion of PPR-800 and PPR-800-N are 92.49% and 87.9%, respectively. Nitrogen doping of RRP involves a two-step carbonization process. In RRP-800-N, nitrogen-containing functional groups (N-6/N-5) decompose and the pores collapse, resulting in decreased thermal stability.[30]

Information on porous materials normally comes from the N_2 adsorption–desorption isotherms of BET analysis, like their specific surface area and porosity. Fig. 3e presents the nitrogen sorption isotherms obtained for both the RRP-800 and its nitrogen-doped counterpart, RRP-800-N. It can be found that the N_2 adsorption–desorption isotherm of RRP-800 is not closed. This is because a majority of biocarbon materials have flexible pores or pores that can only be entered through small necks. After the absorption of the gas, the pore size shrinks. The difficulty in desorption of the adsorbed gas impedes its equilibrium desorption, thereby leading to an incomplete adsorption–desorption curve.[31] RRP-800 exhibits both Type I and Type IV adsorption isotherms. The Type I isotherm is more prominent, indicating that the RRP-800 material possesses a large number of micropores. Because micropores have small pore sizes (typically less than 2 nm), they show a rapid increase in adsorption at low pressures, which then gradually stabilizes, forming an adsorption plateau. RRP-800 has an average pore size of approximately 1.7 nm (as shown in Fig. 3f). The microporous structure provides a large number of sodium-ion storage sites, which is beneficial for enhancing sodium storage capacity. However, an excessive number of micropores can lead to longer ion diffusion paths, especially during high-rate charge–discharge processes, where sodium-ion diffusion is hindered, thus affecting its rate performance.[32] The N_2 adsorption–desorption isotherm of RRP-800-N exhibits the characteristics of a typical Type IV isotherm, accompanied by an H4-type hysteresis loop, indicating that the RRP-800-N material has a mesoporous structure.[33] The mesoporous structure facilitates electrolyte infiltration and provides faster channels for ion transport, thereby improving rate performance. The pore size distribution of the RRP-800-N sample is mainly concentrated in the range of 1–10 nm (as shown in Fig. 3f), consistent with the isotherm analysis results. The mesoporous structure can promote effective contact between the electrode and the electrolyte and provide channels for rapid transport of sodium ions during the charge–discharge process. Table 1 delineates the BET specific surface area and cumulative pore volume for RRP-800 and its derivative, RRP-800-N. While RRP-800-N boasts a specific surface area of 24.18 m^2 g^{-1}, its cousin RRP-800 has a notably higher figure of 162.8 m^2 g^{-1}. Compared to RRP-800, RRP-800-N has a lower BET surface area. However, surface

Table 1   Structural parameters of RRP-800-N and RRP-800

Samples	I_D/I_G	S_{BET} (m² g⁻¹)	Pore volume (cm³ g⁻¹)	Composition (%)		
				C	O	N
RRP-800	1.19	162.58	0.070	85.45	12.11	2.44
RRP-800-N	1.33	24.18	0.025	80.70	15.64	3.66

defects (such as vacancies and edge sites) can preferentially adsorb sodium ions and guide them into the bulk interlayer, shortening the diffusion path. Even though the BET surface area decreases, the active site density per unit area may increase due to the increased number of defects (which can be verified by the Raman ratio of RRP-800-N and RRP-800, where RRP-800-N has more defects compared to RRP-800).[33] The lower specific surface area can reduce side reactions and the formation of a solid electrolyte interface (SEI). This advancement enhances the intercalation capacity of electrodes (ICE), a finding that aligns with the subsequent electrochemical assessments.[34,35]

Elemental composition and distribution studies were conducted via XPS analysis on each sample. C, O and N are present in all the samples. As shown in Table 1, the contents of C, O and N in RRP-800 are 85.45%, 12.11% and 2.44%, respectively, and their contents in RRP-800-N are 80.70%, 15.64% and 3.66%, respectively. The N and O contents of PPR-800-N are significantly higher than those of RRP-800, which indicates that N elements were successfully doped into the C framework of the sample. XPS survey spectrum of RRP-800-N shows three peaks, namely C 1s, N 1s and O 1s peaks. Including one prominent peak (285 eV) and two subtle peaks (398 eV and 531 eV) for binding energies. The XPS survey spectrum of RRP-800 (Fig. 4a) is similar to that of PPR-800-N and shows C, N and O element peaks, with the corresponding binding energies of 284, 398 and 531 eV, respectively. Based on the binding energies of different bonds, the bond composition of each element in RRP-800 and RRP-800-N was fitted, and C 1s and N 1s peaks were

deconvoluted. First, the C 1s spectrum of RRP-800-N was deconvoluted into five components, in Fig. 4b. Similarly, the C 1s of RRP-800 were also fitted into five peaks, which are similar to those of RRP-800-N.[36,37] Second, the various forms of nitrogen in the RRP-800-N material specifically, pyridinic nitrogen at 398.0 eV (N-6), pyrrolic nitrogen at 400.1 eV (N-5), and oxidized nitrogen at 403.2 eV (N-Q) are depicted in Fig. 4c. The comparative abundances of these three nitrogen elements across the two materials are presented in Fig. 4c. The incorporation of N-6 and N-5 within the carbon framework enhances its disorder and conductivity, thereby boosting the sodium-ion storage capabilities.[38,39] RRP-800-N exhibits a combined N-6/N-5 content level of 4.19%, exceeding RRP-800's 2.7% value. Therefore, RRP-800-N has higher disorder and conductivity than RRP-800, which corresponds to the Raman spectral findings. The appearance of the C–N peak proves that N atoms have been successfully injected into the carbon lattice, and defects can be induced by the introduction of N atoms.[23] In N-Q doped systems, sodium ions tend to drift away from the spots where the doping occurred. Conversely, they move toward nitrogen and defect locations in N-5 and N-6 doped systems. In PPR-800-N, N-6 and N-5 enhance surface adsorption and pseudocapacitive adsorption sites. The lone pair electrons of pyridinic nitrogen (N-6) and pyrrolic nitrogen (N-5) form strong coordination with Na⁺, reducing adsorption energy and increasing reversible capacity. N-Q improves the electron conduction network. Graphitic nitrogen (N-Q) is embedded in the carbon skeleton, increasing carrier concentration through n-type doping and reducing polarization losses. N-Q forms a continuous conductive pathway with sp² carbon domains, ensuring rapid charge transport at high current densities.[8] Looking at Fig. 4c, we can see that N-5 and N-6 levels are higher than N-Q levels across all the doped setups, suggesting that sodium ions diffuse more effectively in the doped samples.[40,41]

Therefore, in this work, the prepared *Rosa roxburghii* pomace material was used as an anode for SIBs, and its detailed electrochemical behavior was analyzed. Cyclic voltammograms for RRP-800 and RRP-800-N are presented in Fig. 5a and b. Cyclic voltammetry reveals a redox couple with peak potentials at approximately 1.1 V and 1.3 V in the three cycles of RRP-800-N, a redox couple with peak potentials at approximately 0.9 V and 1.2 V is also observed in RRP-800. This is attributed to the expected intercalation and deintercalation of Na⁺, which indicates that the redox reaction is reversible.[35,42] The higher peak potential after nitrogen doping is because nitrogen doping shrinks sodium ion diffusion channels and reduces lattice strain during charging and discharging.[43] This structural optimization alters the activation energy for sodium-ion insertion/extraction, resulting in an increased peak potential and enhanced cycling stability. Subsequently, a weak oxidation peak appears near 2.0 V for both RRP-800-N and RRP-800. This result confirms that the surface functional groups of both RRP-800 and RRP-800-N undergo irreversible reactions with the electrolyte, which disappears in subsequent scans.[35] The SEI layer's genesis explains this. The initial oxidation peak diminishes in subsequent voltammetric cycles, caused by SEI layer growth and side reactions with surface functional groups during the first
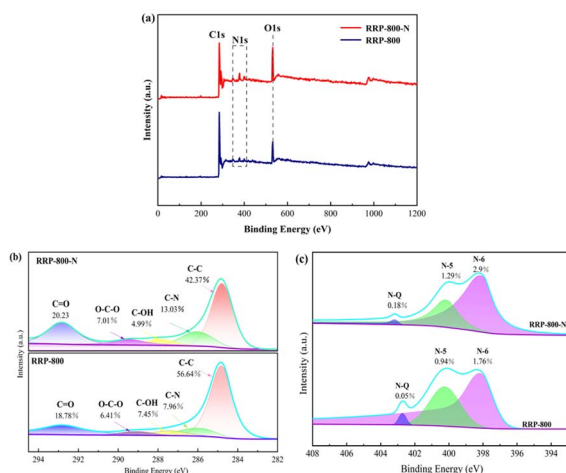

Fig. 4   (a) XPS analytical data; (b) C 1s emission spectra with enhanced resolution; (c) N 1s emission spectra with enhanced resolution.
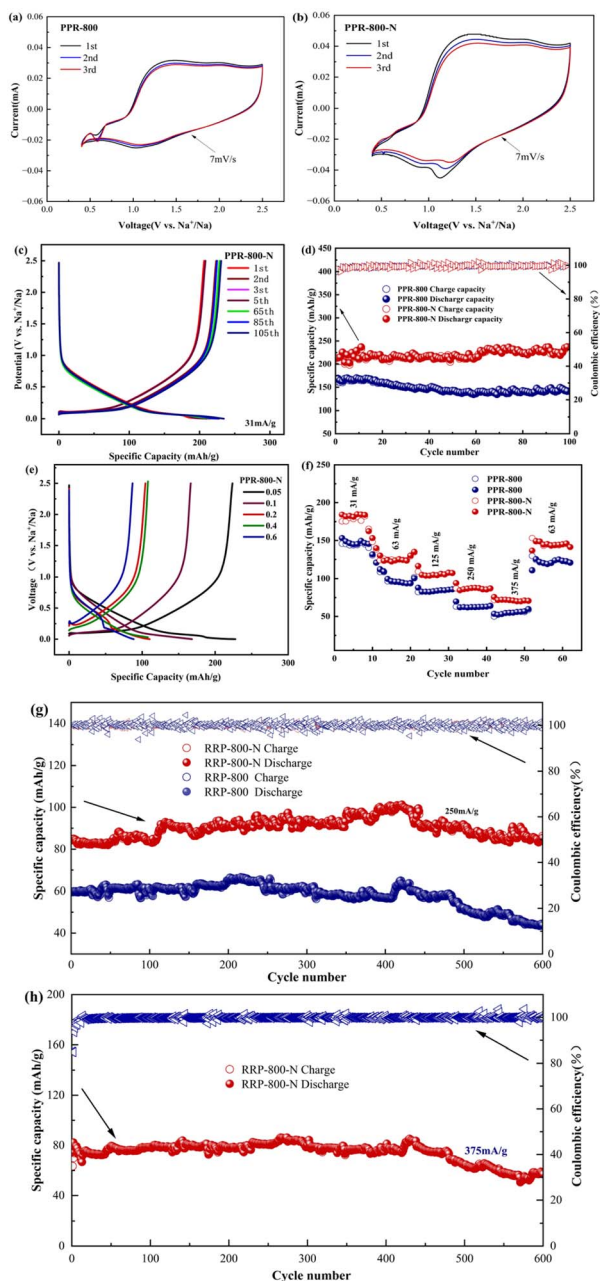
Fig. 5 (a) Cyclic voltammetry (CV) curve of RRP-800; (b) cyclic voltammetry (CV) curve of RRP-800-N; (c) initial GCD profiles at 31 mA g^{-1}; (d) durability studies of the RRP-800-N under repeated cycling; (e) comparative GCD profiles at different current intensities; (f) performance testing at multiple current densities; (g) longevity in cycling at 250 mA g^{-1} charge rate; (h) cycling endurance analysis at a aigher current density of 375 mA g^{-1}.

discharge. The progressive overlap of cyclic voltammograms in later cycles suggests robust cycling stability.[22]

GCD testing showcased the material's electrochemical prowess, as depicted in Fig. 5c. At the 31 mA g^{-1} current load (0.05 mA), the RRP-800-N variant boasts a head start charge capacity of 223.7 mAh g^{-1}, accompanied by an impressive ICE rating of 99.11%. In later cycles, GCD charge–discharge capacity remains stable. The curves show two segments, a sloping region

(0.1–1 V) and a plateau (below 0.1 V). Nitrogen doping in exhibits different capacities.[41,44] RRP-800 displays comparable charge–discharge behavior, exhibiting an initial specific charge capacity of just 160.3 mAh g^{-1} (31 mA g^{-1}) and an ICE of 98.55%. Compared with the RRP-800 electrode, RRP-800-N shows an increase of around 63.4, an improvement of about 40%, in charging capacity. Enhanced slope capacity is attributed to N-doping induced imperfections, per hard carbon's Na$^+$ "adsorption–insertion" storage model, which promotes charge transfer and thereby obtains higher capacity.[45] It can be seen that the ICE of RRP-800-N is far above that of RRP-800. The reason is RRP-800-N has a lower specific surface area after N doping. In general, a lower specific surface area is beneficial to obtaining better discharge capacity at lower rates,[46,47] while reducing side reactions and the formation of SEI, which thereby improves ICE.[48] The cycling performance of RRP-800 and RRP-800-N for Na$^+$ storage is shown in Fig. 5d. The cycling performance curves demonstrate the stability of both electrodes over repeated charge/discharge cycles. Nevertheless, after 100 electrochemical cycles at a current density of 31 mA g^{-1}, the RRP-800 electrode exhibits a reversible specific capacity of 141.6 mAh g^{-1}. Nitrogen doping enhances the electrochemical performance of the RRP-800-N electrode, demonstrates a reversible capacity of 237.1 mAhg^{-1} following 100 cycles at 31 mA g^{-1}. The minimal capacity fade observed can be attributed to the abundance of electrochemically active C–N bonds and the expanded interlayer spacing, facilitating enhanced ion transport.[49] The charge–discharge curve for RRP-800-N exhibits a characteristic profile: a decline leading to a flat section that slowly fades over time. The plateau is indicative of sodium-ion insertion, whereas the sloping portion reflects capacitive behavior. As shown in Fig. 5e, the specific capacity of the RRP-800-N electrode rapidly decreases from the plateau region with the increase of the current, which indicates that the kinetics during Na$^+$ insertion between graphite layers are worse than the surface adsorption kinetics on the active center. Moreover, the rate performance of Na$^+$ storage is also compared in Fig. 5f. RRP-800-N showed reversible specific capacities of 183.8, 135, 107.4, 87.0, and 70.7 mAh g^{-1} at current densities of 0.05, 0.1, 0.2, 0.4, and 0.6 mA, respectively. Looking at electrode cycling stability (Fig. 5g), the RRP-800-N electrode held steady, delivering a reversible specific capacity of 85.4 mAh g^{-1} at a high current density of 250 mA g^{-1}, and continued to perform without a hitch even after a whopping 600 cycles, with a capacity retention rate of 100%. The stability is attributed to the robust construction of the *Rosa roxburghii* pomace material structure. The SEM image shows no significant changes in the morphology and microstructure of RRP-800-N after secondary carbonization. It also shows that the SEI film is relatively complete, which reduces side reactions. Additionally, sodium ions are fully intercalated and deintercalated during charging and discharging, which thereby improves the retention rate. The doping of N atoms reduces polarization. Small polarization leads to relatively high capacity retention rates, and high capacity retention rates break through key technologies like the volume expansion and interface stability of electrode

materials.[50] Fig. 5f reveals a 90% capacity maintained after 600 cycles at 375 mA g^{-1}.

The EIS of electrodes was evaluated to investigate the improvement in Na$^+$ storage performance. As shown in Fig. 6a, RRP-800-N exhibits a smaller semi-circle at medium frequencie. The findings indicate a slight charge transfer takes place subsequent to the formation of the solid-electrolyte interphase (SEI) layer. The interfacial charge transfer resistance remains nearly constant, pointing to the development of an exceptionally thin yet robust SEI layer finding that aligns perfectly with the earlier cyclic voltammetry results. The formation of the SEI layer and the stability of this interfacial layer directly suppress electrolyte decomposition and electrode structure degradation, thereby significantly enhancing the long-term cycling performance of the electrode.[51] Introducing nitrogen atoms into a carbon structure generally increases the material's electrical conductivity, as nitrogen doping can alter the electronic structure of carbon by introducing additional charge carriers or forming conductive hybridized orbitals. The charge transfer resistance (R_{ct}) is typically related to the interfacial charge transfer process between the electrode material and the electrolyte. Nitrogen doping reduces R_{ct} by providing more active sites or improving the material's conductivity. Functional groups like pyridinic nitrogen and pyrrolic nitrogen act as active sites, promoting electron transfer and thus reducing charge transfer resistance. Regarding ion diffusion behavior, nitrogen doping affects the interlayer spacing of carbon materials, such as expanding the interlayer spacing, thereby promoting ion insertion and extraction.[52] Additionally, it

reinforces the structural integrity of the carbon matrix, ensuring remarkable long-term cycling stability.[53,54] Cyclic voltammetry elucidates biomass carbon's charge storage. Recognizing that Na$^+$ storage comprises both surface capacitive contributions and bulk diffusion-limited processes, CV measurements were conducted on RRP-800-N at varying scan rates (Fig. 6b). The follow the following relationship:[55,56]

$$i = av^b \quad (1)$$

The parameters a and b can be derived *via* linear regression analysis of the experimental data.[34] eqn (1) can be rewritten as:

$$\log(i) = \log(a) + b\log(v) \quad (2)$$

Drawing from the given equation, where a and b serve as key parameters, b can be derived through computational analysis. Typically falling between 0.5 and 1.0, the magnitude of b serves as an indicator of how strongly diffusion control and capacitive effects govern the charge–discharge cycle. A value nearing 1.0 suggests near-ideal capacitive performance, highlighting efficient energy storage dynamics. The values of b corresponding to peak 1 and peak 2 for PPR-800-N are 0.78 and 0.96, respectively (Fig. 6c). RRP-800-N charge retention appears governed by both surface and diffusion dynamics.[57] Nitrogen doping in RRP-800-N enables the efficient synergy of capacitive and diffusion-controlled sodium storage mechanisms through enhanced surface pseudocapacitive activity and optimized bulk diffusion kinetics. This balance allows the material to achieve an optimum between high energy density (dominated by diffusion mechanism) and high power density (dominated by capacitive mechanism), thereby significantly improving the overall performance of SIBs.[58] Capacitive activity percentage is quantifiable *via*:

$$i = k_1v + k_2v^{1/2} \quad (3)$$

The capacitive behavior of the current ($k^{-1}v$) can be quantified at a fixed potential, where k represents a constant. As illustrated in Fig. 6d, RRP-800-N shows capacitive behavior accounting for 89% at 5 mV s^{-1}. When the scan rate increases, the diffusion-controlled contribution diminishes, while the capacitive effect becomes more dominant. Slower scan rates favor capacitive behavior associated with diffusion-limited redox processes. Fig. 6e demonstrates that as the scan rate climbs from 1 to 7 mV s^{-1} specifically at 1, 3, 5, and 7 mV s^{-1} the progressive rise in capacitive contribution reflects enhanced kinetic performance in the material. The capacitive contributions of RRP-800-N are 64%, 85%, 89% and 93%, respectively. This indicates that RRP-800-N mainly stores Na$^+$ through an adsorption mechanism and absorbs and releases Na$^+$, which results in good cycling stability.
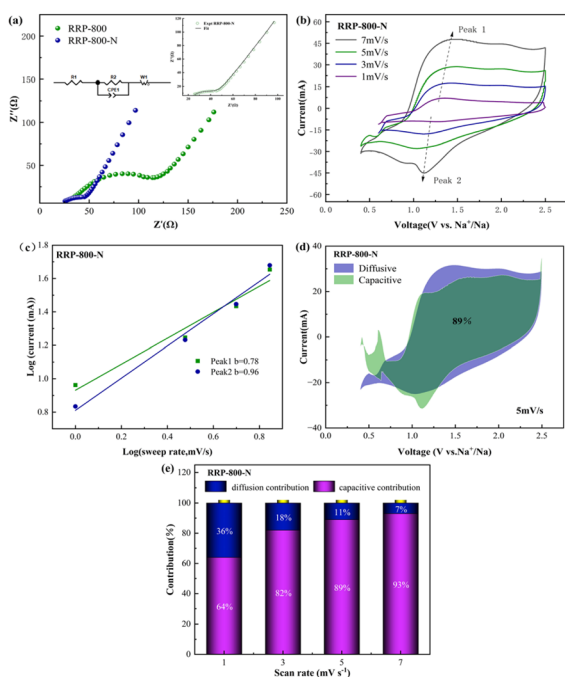

Fig. 6 (a) EIS plots. The inset is the fitting plot of RRP-800-N; (b) CV curves of RRP-800-N at different scan rates; (c) measurement of *b*-values of RRP-800-N; (d) contribution ratio of capacitance of RRP-800-N; (e) contribution ratio of capacitance of RRP-800-N at different scan rates.

4 Conclusions

In summary, a scalable and versatile method was reported to prepare N-doped hierarchical porous hard carbon using the

Rosa roxburghii pomace as a precursor through simple carbonization and doping. Melamine as a nitrogen source was introduced into the *Rosa roxburghii* pomace. The expanded interlayer spacing and numerous active sites of RRP-800-N compared to RRP-800 are beneficial to the diffusion and transport of sodium ions and electrons. Beyond that, the doping of N changes the surface properties of the carbon, which enables the carbon to have a faster capacitive energy storage capacity than Na$^+$. Electrochemical studies showed good electrochemical performance and came to the following conclusions:

(1) The RRP-800-N exhibits exceptional electrochemical performance: a large interlayer spacing (0.69 nm), a high reversible capacity (223.7 mAh g^{-1} at 31 mA g^{-1}), an excellent initial coulombic efficiency (99.11%). Notably, it demonstrates 100% capacity retention over 100 cycles and maintains 85.4 mAh g^{-1} at 250 mA g^{-1}. Even after 600 cycles, 100% capacity retention is sustained.

(2) The abundance of highly active nitrogen functionalities and the disordered amorphous structure of RRP-800-N contribute to a high density of electrochemically active sites and enhanced electronic conductivity. The abundant mesopores provide continuous ion transport pathways, shortening the diffusion distance of Na$^+$ from the electrolyte to the bulk material.

(3) While nitrogen-doped carbon anodes derived from *Rosa roxburghii* pomace show excellent initial coulombic efficiency and cycle durability in sodium-ion batteries, their weight-based capacity still falls short of ideal. Moving forward, research efforts will focus on optimizing the material's architecture to boost its energy storage performance.

The RRP-800-N electrode demonstrates exceptional initial coulombic efficiency and robust cycling performance in sodium-ion batteries, achieved *via* a straightforward synthesis method. This approach not only offers a viable pathway for engineering high-performance heteroatom-doped carbon materials but also presents an economical and sustainable solution for developing next-generation electrode materials in renewable energy applications.

Data availability

The data supporting this article are all included in the manuscript.

Author contributions

Fangli Lou conducted the experiment, data analysis and collation, and wrote the manuscript, Jinju Wang and Xiang Wang guided the experiment, Mingxian Zhang commanded the operation of the experimental instruments, and Jie Yuan revised the first draft and provided financial support.

Conflicts of interest

The authors declare that there is no conflict of interest regarding the publication of this paper.

Acknowledgements

Notes and references

1 Z.-L. Xu, J. Park, G. Yoon, H. Kim and K. Kang, *Small Methods*, 2019, **3**, 1800227.
2 T. Li, C. Chen, A. H. Brozena, J. Y. Zhu, L. Xu, C. Driemeier, J. Dai, O. J. Rojas, A. Isogai, L. Wågberg and L. Hu, *Nature*, 2021, **590**, 47–56.
3 J. He, C. Lu, H. Jiang, F. Han, X. Shi, J. Wu, L. Wang, T. Chen, J. Wang, Y. Zhang, H. Yang, G. Zhang, X. Sun, B. Wang, P. Chen, Y. Wang, Y. Xia and H. Peng, *Nature*, 2021, **597**, 57–63.
4 Y. Xu, C. Zhang, M. Zhou, Q. Fu, C. Zhao, M. Wu and Y. Lei, *Nat. Commun.*, 2018, **9**, 1720.
5 Y. B. Rao, K. K. Bharathi and L. N. Patro, *Solid State Ionics*, 2021, **366–367**, 115671.
6 M. Thompson, Q. Xia, Z. Hu and X. S. Zhao, *Mater. Adv.*, 2021, **2**, 5881–5905.
7 M. Chen, Q. Liu, Z. Hu, Y. Zhang, G. Xing, Y. Tang and S.-L. Chou, *Adv. Energy Mater.*, 2020, **10**, 2002244.
8 B. Lu, C. Lin, H. Xiong, C. Zhang, L. Fang, J. Sun, Z. Hu, Y. Wu, X. Fan, G. Li, J. Fu, D. Deng and Q. Wu, *Molecules*, 2023, **28**, 4027.
9 H. Li, K. Wang, S. Cheng and K. Jiang, *ACS Appl. Mater. Interfaces*, 2018, **10**, 8016–8025.
10 Z. Tang, S. Zhou, Y. Huang, H. Wang, R. Zhang, Q. Wang, D. Sun, Y. Tang and H. Wang, *Electrochem. Energy Rev.*, 2023, **6**, 8.
11 H. Liu, M. Jia, N. Sun, B. Cao, R. Chen, Q. Zhu, F. Wu, N. Qiao and B. Xu, *ACS Appl. Mater. Interfaces*, 2015, **7**, 27124–27130.
12 X. Lei, L. Zhang, X. Guo, Q. Tian, X. Fan, H. Tong and Y. Yang, *J. Energy Storage*, 2024, **101**, 113792.
13 F. Wu, L. Liu, Y. Yuan, Y. Li, Y. Bai, T. Li, J. Lu and C. Wu, *ACS Appl. Mater. Interfaces*, 2018, **10**, 27030–27038.
14 N. Zhang, Q. Liu, W. Chen, M. Wan, X. Li, L. Wang, L. Xue and W. Zhang, *J. Power Sources*, 2018, **378**, 331–337.
15 J. Xiang, W. Lv, C. Mu, J. Zhao and B. Wang, *J. Alloys Compd.*, 2017, **701**, 870–874.
16 L. Cao, W. Hui, Z. Xu, J. Huang, P. Zheng, J. Li and Q. Sun, *J. Alloys Compd.*, 2017, **695**, 632–637.
17 J. Deng, M. Li and Y. Wang, *Green Chem.*, 2016, **18**, 4824–4854.
18 M. Li, Y. Wang, Y. Zhang and N. Zhang, *Chem. Eng. J.*, 2025, **506**, 160083.
19 L. Pei, H. Cao, L. Yang, P. Liu, M. Zhao, B. Xu and J. Guo, *Ionics*, 2020, **26**, 5535–5542.
20 F. Xie, Z. Xu, A. C. S. Jensen, F. Ding, H. Au, J. Feng, H. Luo, M. Qiao, Z. Guo, Y. Lu, A. J. Drew, Y.-S. Hu and M.-M. Titirici, *J. Mater. Chem. A*, 2019, **7**, 27567–27575.

21 I. Jeon, T. Kim, J. Seo, I.-K. Jeong, J. H. Lee, M. Park, Y. Park, D. Yang and C. R. Cho, *Appl. Surf. Sci.*, 2024, **648**, 159023.

22 D. Zhang, Y. Chen, X. Zheng, P. Liu, L. Miao, Y. Lv, Z. Song, L. Gan and M. Liu, *Angew. Chem., Int. Ed.*, 2025, **64**, e202500380.

23 C. Nita, B. Zhang, J. Dentzer and C. Matei Ghimbeu, *J. Energy Chem.*, 2021, **58**, 207–218.

24 L. Gao, C. Zhang, M. Cao, J. Li and L. Xiong, *Diamond Relat. Mater.*, 2023, **140**, 110562.

25 N. Sun, Z. Guan, Y. Liu, Y. Cao, Q. Zhu, H. Liu, Z. Wang, P. Zhang and B. Xu, *Adv. Energy Mater.*, 2019, **9**, 1901351.

26 M. Kim, J. F. S. Fernando, Z. Li, A. Alowasheeir, A. Ashok, R. Xin, D. Martin, A. Kumar Nanjundan, D. V. Golberg, Y. Yamauchi, N. Amiralian and J. Li, *Chem. Eng. J.*, 2022, **445**, 136344.

27 M. Dahbi, M. Kiso, K. Kubota, T. Horiba, T. Chafik, K. Hida, T. Matsuyama and S. Komaba, *J. Mater. Chem. A*, 2017, **5**, 9917–9928.

28 Y. Wang, Z. Feng, W. Zhu, V. Gariépy, C. Gagnon, M. Provencher, D. Laul, R. Veillette, M. L. Trudeau, A. Guerfi and K. Zaghib, *Materials*, 2018, **11**, 1294.

29 T. Shi, Z. Song, C. Hu, Q. Huang, Y. Lv, L. Miao, L. Gan, D. Zhu and M. Liu, *Angew. Chem.*, 2025, e202501278.

30 J. Tamuly, D. Bhattacharjya and B. K. Saikia, *Energy Fuels*, 2022, **36**, 12847–12874.

31 K. Schutjajew, J. Pampel, W. Zhang, M. Antonietti and M. Oschatz, *Small*, 2021, **17**, 2006767.

32 X. Yang, C. Hu, Y. Chen, Z. Song, L. Miao, Y. Lv, H. Duan, M. Liu and L. Gan, *J. Energy Storage*, 2024, **104**, 114509.

33 P. Luo, Z. Huang and X. Ma, *J. Alloys Compd.*, 2025, **1024**, 180259.

34 X. Chen, S. Wei, J. Wang, F. Tong, T. Söhnel, G. I. N. Waterhouse, W. Zhang, J. Kennedy and M. P. Taylor, *Intermetallics*, 2024, **169**, 108306.

35 F. S. Genier, S. Pathreeker, R. L. Schuarca, M. Islam and I. D. Hosein, *ECS Adv.*, 2022, **1**, 030502.

36 E. Demir, M. Aydin, A. A. Arie and R. Demir-Cakan, *J. Alloys Compd.*, 2019, **788**, 1093–1102.

37 R. R. Gaddam, A. H. F. Niaei, M. Hankel, D. J. Searles, N. A. Kumar and X. S. Zhao, *J. Mater. Chem. A*, 2017, **5**, 22186–22192.

38 L. Chen, L. Bai, J. Yeo, T. Wei, W. Chen and Z. Fan, *ACS Appl. Mater. Interfaces*, 2020, **12**, 27499–27507.

39 Z.-Y. Gu, J.-Z. Guo, X.-X. Zhao, X.-T. Wang, D. Xie, Z.-H. Sun, C.-D. Zhao, H.-J. Liang, W.-H. Li and X.-L. Wu, *InfoMat*, 2021, **3**, 694–704.

40 Z. Yan, Q.-W. Yang, Q. Wang and J. Ma, *Chin. Chem. Lett.*, 2020, **31**, 583–588.

41 S. Huang, Z. Li, B. Wang, J. Zhang, Z. Peng, R. Qi, J. Wang and Y. Zhao, *Adv. Funct. Mater.*, 2018, **28**, 1706294.

42 P. Bai, Y. He, X. Zou, X. Zhao, P. Xiong and Y. Xu, *Adv. Energy Mater.*, 2018, **8**, 1703217.

43 X. Zhu, X. Jiang, X. Liu, L. Xiao and Y. Cao, *Green Energy Environ.*, 2017, **2**, 310–315.

44 K. Guo, Z. Song, Y. Lv, L. Gan and M. Liu, *Adv. Funct. Mater.*, 2025, 2506036.

45 Y. Huang, Y. Wang, P. Bai and Y. Xu, *ACS Appl. Mater. Interfaces*, 2021, **32**, 38441–38449.

46 R.-M. Gao, Z.-J. Zheng, P.-F. Wang, C.-Y. Wang, H. Ye and F.-F. Cao, *Energy Storage Mater.*, 2020, **30**, 9–26.

47 X. Zhang, X. Dong, X. Qiu, Y. Cao, C. Wang, Y. Wang and Y. Xia, *J. Power Sources*, 2020, **476**, 228550.

48 W. Deng, Y. Cao, G. Yuan, G. Liu, X. Zhang and Y. Xia, *ACS Appl. Mater. Interfaces*, 2021, **13**, 47728–47739.

49 Y. B. Rao, Y. Saisrinu, S. Khatua, K. K. Bharathi and L. N. Patro, *J. Alloys Compd.*, 2023, **968**, 171917.

50 J. Zhang, D.-W. Wang, W. Lv, L. Qin, S. Niu, S. Zhang, T. Cao, F. Kang and Q.-H. Yang, *Adv. Energy Mater.*, 2018, **8**, 1801361.

51 G. Zhang, Y. Zhao, L. Yan, L. Zhang and Z. Shi, *J. Mater. Sci.: Mater. Electron.*, 2021, **32**, 5645–5654.

52 W. Ma, L. Yu, X. Miao, X. An, J. Zhang, Q. Kong, Q. Wang and W. Yao, *Adv. Funct. Mater.*, 2025, 2421790.

53 Q. Tao, H. Ding, H. Zhao, J. Huang, B. Dai and J. Li, *J. Alloys Compd.*, 2024, **976**, 172977.

54 Y. Jin, Y. Xu, P. M. L. Le, T. D. Vo, Q. Zhou, X. Qi, M. H. Engelhard, B. E. Matthews, H. Jia, Z. Nie, C. Niu, C. Wang, Y. Hu, H. Pan and J.-G. Zhang, *ACS Energy Lett.*, 2020, **5**, 3212–3220.

55 M. Ma, H. Cai, C. Xu, R. Huang, S. Wang, H. Pan and Y.-S. Hu, *Adv. Funct. Mater.*, 2021, **31**, 2100278.

56 H. Yu, L. Shang, T. Bian, R. Shi, G. I. N. Waterhouse, Y. Zhao, C. Zhou, L.-Z. Wu, C.-H. Tung and T. Zhang, *Adv. Mater.*, 2016, **28**, 5140.

57 J. K. Mathiesen, R. Väli, M. Härmas, E. Lust, J. F. von Bülow, K. M. Ø. Jensen and P. Norby, *J. Mater. Chem. A*, 2019, 7, 11709–11717.

58 Z. Li, L. Cai, K. Chu, S. Xu, G. Yao, L. Wei and F. Zheng, *Dalton Trans.*, 2021, **50**, 4335–4344.